LANGMUIR

pubs.acs.org/Langmuir Article

In Situ Growth of Cationic Covalent Organic Frameworks (COFs) for Mixed Matrix Membranes with Enhanced Performances

Xingyuan Wang, Xiansong Shi, and Yong Wang*

Cite This: *Langmuir* 2020, 36, 10970−10978 Read Online

ACCESS | Metrics & More | Article Recommendations | Supporting Information

ABSTRACT: Covalent organic frameworks (COFs) are increasingly utilized as doping agents for the design of advanced ultrafiltration mixed matrix membranes, thanks to their prominent nanoporosity and excellent polymer compatibility. However, current strategies are largely limited in the complicated postaddition of neutral COF particulates. Herein, cationic COFs, namely, TpEB, with sizes down to ∼39 nm are *in situ* synthesized in polyacrylonitrile (PAN) solution as crystalline fillers for the production of highly permeable TpEB−PAN ultrafiltration membranes. After the condensation of monomer pairs, the growth of cationic TpEB crystallites is restrained due to the electrostatic interaction with negatively charged PAN chains, leading to the formation of a homogeneous TpEB-incorporated casting solution. During the subsequent nonsolvent-induced phase separation process, TpEB crystallites facilitate exchange between the solvent and the nonsolvent because of their hydrophilic and nanoporous nature, accelerating the rate of phase inversion to form a highly porous membrane surface. Thus-prepared TpEB−PAN membranes deliver a tight rejection of BSA with water permeance of up to 380 L m^{-2} h^{-1} bar^{-1}, which is 35.6% higher than that of the original PAN membranes prepared without TpEB. The TpEB−PAN membranes also exhibit enhanced operation stabilities and fouling resistances. This *in situ* growth strategy suggests a new avenue for the preparation of advanced mixed matrix membranes.

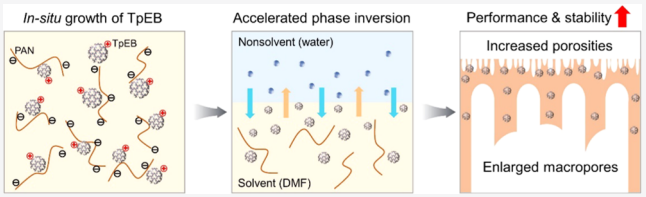

INTRODUCTION

Since the dawn of covalent organic frameworks (COFs) in the year of 2005,[1] great attention has been paid to this novel kind of nanoporous organic materials. As porous crystalline polymers, COFs are constructed by linking various types of organic building blocks through strong covalent bonds.[2−6] Compared to other polymers, COFs have readily access to tailored functions and possess highly order structures with size-tunable nanopores,[7,8] endowing them with abundant attractive merits, such as high porosities, good stabilities, and large surface areas.[9,10] Therefore, COFs are extensively applied in various areas, including separation, storage, catalysis, adsorption, *etc.*[11−14]

Benefiting from their homopores with adjustable sizes ranging from ∼0.5 to 4.7 nm, COFs have shown promising applications in membrane-based separations including nanofiltration,[15,16] ultrafiltration,[17] and pervaporation.[18] However, COFs usually appear in the form of micron-sized particulates that are hard to be processed, making them difficult to be directly employed in membrane separations. Given this, several strategies have been developed to overcome this obstacle, such as solvothermal growth,[19] interfacial crystallization,[20] self-assembly of COF nanosheets,[15] and casting and baking.[12] Due to their relatively small pore sizes, COFs are extensively investigated as the precursors to construct nanofiltration membranes to realize the separation of ions and dyes.[15−17] To meet the demand for different separation accuracies, such as the processes of biomolecule purification, cell separation, and hemodialysis, which mainly rely on the membrane with relatively larger pore sizes,[21] it is highly necessary to expand the application of COFs in ultrafiltration. Considering that the fully organic nature of COFs gives them better affiliation and compatibility to the polymer matrix,[22] COFs present great potential in becoming excellent fillers to produce COF-based ultrafiltration mixed matrix membranes (MMMs) with enhanced performances.[11,23]

Typically, the method of incorporating micron-sized COF particulates in the casting solution to produce COF-based MMMs *via* nonsolvent-induced phase separation (NIPS) has been reported.[24,25] Due to the operation facileness, NIPS is one of the most adopted methods to produce ultrafiltration membranes. In this process, a nonsolvent for a polymer is introduced to a homogeneous polymer solution to demix the solution into two phases: a polymer-rich phase that turns into the matrix of membranes after coagulation and a polymer-poor phase that forms membrane pores after it is removed from the precipitated solution.[26−28] Pure polymer membranes usually suffer from undesirable performances due to their relatively

Received: June 10, 2020
Revised: August 30, 2020
Published: August 31, 2020

https://dx.doi.org/10.1021/acs.langmuir.0c01714
Langmuir 2020, 36, 10970−10978

Scheme 1. Schematic Representation of the Synthesis of TpEB

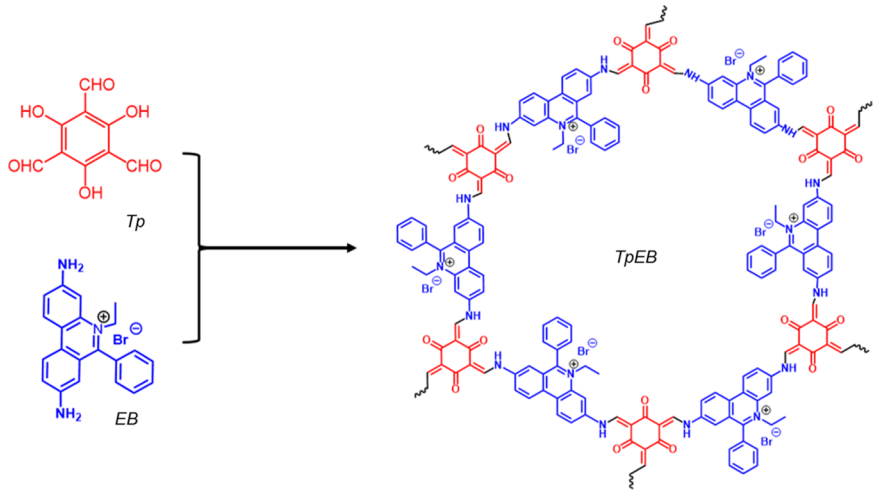

low pore density and hydrophilicity, and therefore, modification processes, such as the blending method, are often required.[29,30] For instance, Gao and co-workers blended microwave-synthesized COFs of TpPa-2 into a polysulfone/poly(ethylene glycol) solution to produce COF-incorporated MMMs with enhanced ultrafiltration performances.[25] However, this postaddition method of blending presynthesized COF particulates into the polymer solution for NIPS may result in poor dispersion of COFs in the casting solution due to their relatively large particle sizes. Therefore, the membranes fabricated through this strategy may have nonuniform structures or defects, even with the loss of COFs during membrane preparation, which prevents the further improvement of membrane performances.[31,32] Also, the postadditon method involves tedious synthesis processes of COF particulates with harsh conditions, such as high temperatures and toxic solvents, and long synthesis durations, which greatly hinder their scalability. Therefore, it is greatly desired to develop an effective methodology to produce COF-based MMMs to take full advantage of the superiority of COFs in ultrafiltration.

In this work, a facile *in situ* growth strategy has been explored to produce highly permeable COF-based ultrafiltration MMMs. Instead of postadding COF particulates, a cationic COF of TpEB has been *in situ* synthesized by blending monomers and the catalyst into the polyacrylonitrile (PAN) solution to produce TpEB−PAN membranes. The electrostatic interaction between the cationic TpEB and the negatively charged PAN chains restrains the size of TpEB crystallites grown in the casting solution. Thus-synthesized TpEB crystallites with sizes down to ∼39 nm are well dispersed, producing a homogeneous and stable TpEB-incorporated casting solution. The intrinsic homopores and high hydrophilicity of TpEB endow the resultant membranes with enhanced water permeance as well as high protein rejections. Thus-prepared TpEB−PAN membranes also present improved operation stability and fouling resistance, which shows the superiority of this *in situ* growth strategy in preparing ultrafiltration MMMs with enhanced performances.

EXPERIMENTAL SECTION

Materials. Commercially available polyacrylonitrile (PAN, 85 kDa) and a polypropylene (PP) nonwoven support obtained from Shanghai Jiujun Tech Co. were used to produce ultrafiltration membranes. TpEB monomers 2,4,6-triformylphloroglucinol (Tp, 98%) and ethidium bromide (EB, 98%) were purchased from Jilin Yanshen Technology Co. Ltd. and Macklin Co., respectively. *N*,*N*-dimethylformamide (DMF, 99.9%), mesitylene (98%), 1,4-dioxane (99%), *p*-phenylenediamine (Pa, 97%), and benzidine (BD, 95%) were supplied by Aladdin. Acetic acid (AA, 99%) was obtained from Shanghai Shenbo Chemical Co. Ltd. Bovine serum albumin (BSA, 66 kDa) and phosphate-buffered saline (PBS) tablets were purchased from MP Biomedicals. Deionized water (DI water; conductivity, 8−20 μs cm^{-1}) was used in all tests. All chemicals were used without further purification.

Synthesis of Micron-Sized TpEB Particulates. The preparation of micron-sized TpEB particulates was conducted using the traditional thermal synthesis method (Scheme 1).[33,34] Specifically, 0.2 mmol Tp (0.042 g) and 0.3 mmol EB (0.118 g) were added into a pyrex tube (10 × 8 mm^2 and length 18 cm) followed by pouring the mixture solvent (5 mL of 1,4-dioxane and 5 mL of mesitylene). After the sonication treatment for 10 min, 200 μL of 6 mol L^{-1} AA was added into the tube as the catalyst, and the obtained solution was sonicated for another 10 min. Then, the tube was flash-frozen at 77 K (liquid N_2 bath) and degassed by freeze−pump−thaw cycles three times. The tube was sealed and then heated at 120 °C for 3 days. A dark red precipitate was obtained by filtration, washed with ethanol, and dried at 80 °C overnight to get the TpEB particulates.

Fabrication of TpEB−PAN Ultrafiltration MMMs. TpEB−PAN ultrafiltration MMMs were prepared following the NIPS method.[24] The fabrication started with dissolving PAN powders in DMF at 70 °C with a concentration of 14 wt %. After sufficient dissolution, the monomer pairs (Tp and EB) and 5 μL of AA as the catalyst were added into the PAN solution, and the mass concentrations of monomer pairs were varied from 0 to 0.09 wt %. The thus-prepared solution was stirred at 70 °C for 3 h so that the *in situ* formed TpEB was uniformly distributed in the PAN solution. To ensure that the TpEB possesses the desired crystallinity, the TpEB-incorporated PAN solution was then heated at 70 °C for 12 h without stirring. Subsequently, the solution was kept in a vacuum oven overnight to remove residual air bubbles, after which the casting solution was obtained. The resultant solution was then cast onto a PP nonwoven support using a casting knife with a gate height of 300 μm, which was then immersed into DI water for the solvent−nonsolvent exchange at room temperature. The resultant TpEB−PAN membranes were thoroughly washed and stored in DI water. Thus-prepared membranes were denoted TpEB$_X$−PAN membranes, in which *X* stands for the concentration of monomer pairs. (For example, TpEB$_3$−PAN membrane stands for the TpEB−PAN membrane with 0.03 wt % of monomer pairs.) To give a comparison, we also prepared the TpEB−PAN membranes by postadding micron-sized TpEB particulates to the PAN solution followed by the NIPS process.

https://dx.doi.org/10.1021/acs.langmuir.0c01714
Langmuir 2020, 36, 10970−10978

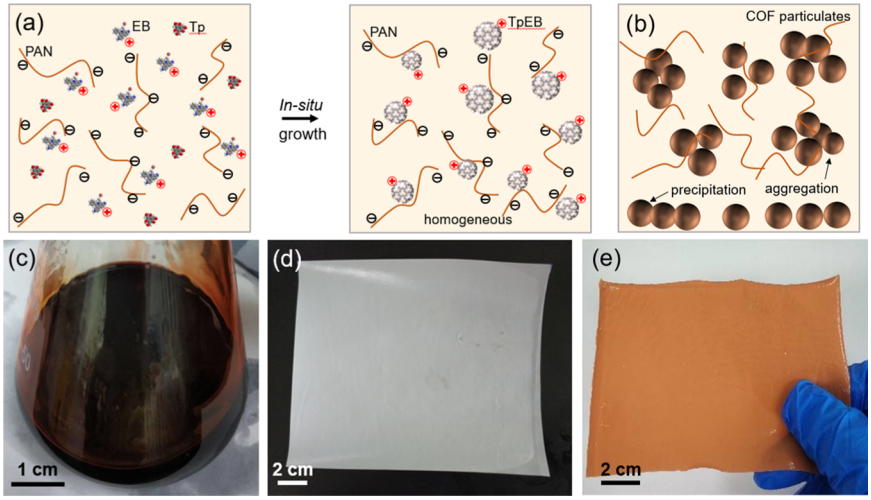

Figure 1. Preparation of TpEB−PAN membranes *via* an *in situ* growth strategy. (a) Diagram for the *in situ* growth of nanosized TpEB in the PAN solution, (b) diagram for the postaddition of micron-sized COF particulates, (c) digital image of the casting solutions obtained from *in situ* growth, and digital images of the (d) original PAN membrane and (e) prepared TpEB−PAN membrane.

Besides, two kinds of COF−PAN membranes containing negatively charged COFs, namely, TpPa and TpBD, were also fabricated using the same *in situ* growth strategy. The self-standing TpEB−PAN membranes without the nonwoven fabric support were also prepared by directly casting the polymer solution onto a glass plate using the same method as described above.

Characterizations. The X-ray diffraction (XRD) patterns of membranes and TpEB particulates were measured at room temperature by a Rigaku Smart Lab X-ray diffractometer with Cu Kα radiation (λ = 0.15418 nm) at 2θ of 2−40° with a step of 0.02° s^{-1}. Fourier transform infrared (FT-IR) spectroscopy measurements were performed on a Nicolet 8700 infrared spectrometer with the wavenumber ranging from 5000 to 500 cm^{-1}. Attenuated total reflection (ATR) mode was used for membrane tests, and the potassium bromide (KBr) pressed pellet method was used for particulate tests. The surface and cross-sectional morphologies of the membranes were characterized by a field-emission scanning electron microscope (SEM, Hitachi S-4800) at an accelerating voltage of 3 kV after sputter-coating with a thin layer of platinum. For the membrane surface, the nonwoven-supported ultrafiltration membranes were coated for 30 s before imaging; for cross-sectional imaging, the self-standing membranes were fractured in liquid nitrogen and then coated for 45 s. At least 200 pores on the surface SEM image of each sample were measured using software NanoMeasurer to estimate average pore sizes and pore density. An energy-dispersive X-ray spectrometer (EDS, EMAX X-act) was used to detect the element distribution of the membrane surface. Atomic force microscopy (AFM, XE-100, Park Systems) was utilized to obtain the topography profiles and surface roughness of the membranes. The water contact angles (WCAs) of the membranes were obtained using a contact angle goniometer (DropMeter A100, Maist). The ζ-potential of the membrane surface was measured by an electrokinetic analyzer (SurPASS, Anton Paar, Austria) using a 1 mmol L^{-1} potassium chloride (KCl) aqueous solution as an electrolyte solution. The fluorescence microscopy images of the membranes were obtained using a confocal microscope (Edinburgh FLS980).

Filtration Tests. The water transport property and separation performance tests were performed at room temperature under a transmembrane pressure of 1 bar using a multicell cross-flow apparatus at a flow rate of 50 L min^{-1} with an effective membrane area of 7.07 cm^2.

Pure water permeance (L m^{-2} h^{-1} bar^{-1}) and protein rejection (%) of 0.5 g L^{-1} of BSA were measured to evaluate the performance of the membranes. The water permeance was calculated by the following equation

$$\text{water permeance} = V/(AtP) \quad (1)$$

where V (L) stands for the volume of DI water that goes across the effective area A (m^2) of the membrane in a predetermined time t (h) under the transmembrane pressure P (bar).

Membrane selectivities were evaluated from the protein separation ability of membranes using 0.5 g L^{-1} BSA in the PBS aqueous solution as a feed. The protein rejection (%) was calculated as

$$\text{rejection} = (1 - C_p/C_f) \times 100\% \quad (2)$$

where C_p and C_f are the BSA concentrations in the permeate and the feed, respectively. The BSA concentration was determined by a UV−vis absorption spectrometer (NanoDrop 2000C) at a wavelength of 280 nm.

Performance Stability Tests. The above filtration tests were performed for as long as 12 h to evaluate the operation stability of the membranes. The dynamic BSA filtration tests were performed under 1 bar to evaluate the antifouling competence of the membranes. DI water and the BSA solution were filtrated alternately through the membrane for three cycles in a cross-flow filtration module. The membranes were cleaned by thoroughly washing the membrane surface with the PBS buffer solution several times at the end of each BSA filtration. The flux recovery ratio (FRR) is calculated as

$$\text{FRR} = F/F_0 \times 100\% \quad (3)$$

where F_0 is the original water permeance of the membrane and F is the water permeance after each cycle.

RESULTS AND DISCUSSION

Upon condensation of monomer pairs, TpEB oligomers quickly generate in the PAN solution due to the high reactivity between the aldehyde groups (−CHO) of Tp and the amino groups ($-NH_2$) of EB. Notably, the positively charged monomer EB endows the formed TpEB oligomers with the same positive charge. Moreover, known as one of the pseudohalogens, the cyano groups (−CN) in the PAN chains possess strong electron absorption ability to form negative charge centers and endow the PAN chains with negative charges.[35] Therefore, the positively charged TpEB oligomers interact with the negatively charged PAN chains *via* electrostatic attraction, restraining their further growth into macro-sized particulates. Also, the high viscosity of the PAN solution suppresses the mobility of monomer pairs and the resulting TpEB oligomers, which prevents the possible aggregation. The

https://dx.doi.org/10.1021/acs.langmuir.0c01714
Langmuir 2020, 36, 10970−10978

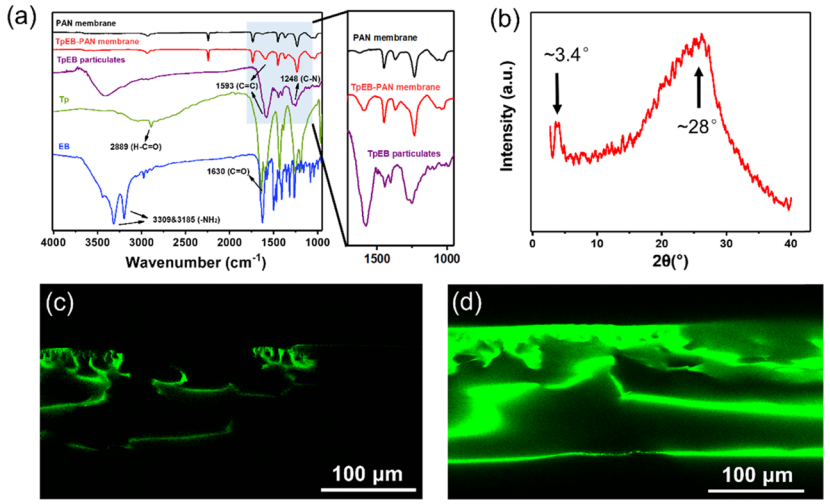

Figure 2. Characterizations of the TpEN−PAN membranes. (a) FT-IR spectra of the TpEB−PAN membrane with 1 wt % monomer pairs in the casting solution, PAN membrane, TpEB particulates, and monomer pairs; (b) XRD pattern of TpEB nanoparticles collected from the membrane; and fluorescence microscopy images of the (c) PAN membrane and (d) $TpEB_5$−PAN membrane.

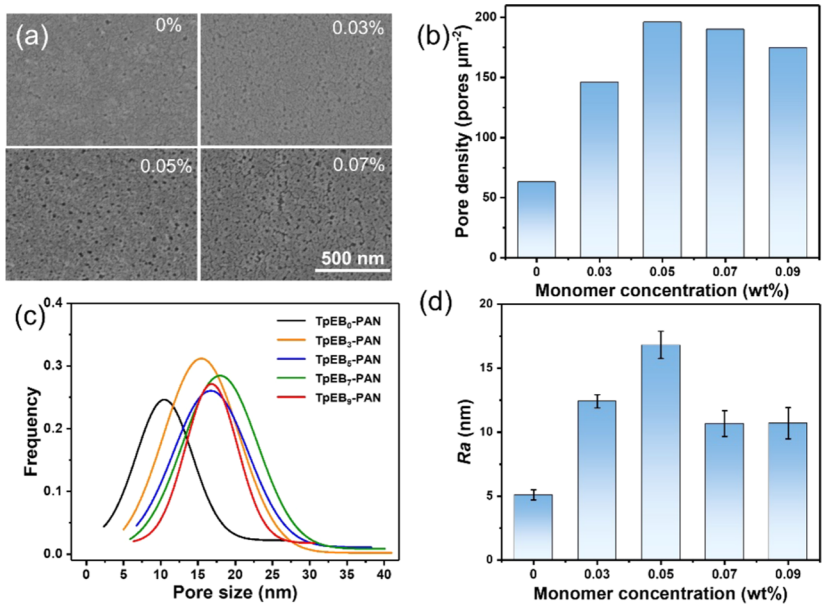

Figure 3. Investigation into the structures of TpEB−PAN membranes with various monomer concentrations. (a) Surface morphologies and the scale bar applied to all SEM images, (b) surface pore density, (c) pore size distribution, and (d) surface roughness.

relatively small sizes as well as the interaction with PAN chains contribute to the formation of a homogeneous casting solution with well-dispersed nanosized TpEB crystallites (Figure 1a). In contrast, the postaddition of micron-sized COF particulates usually results in the formation of a labile casting solution with aggregation and precipitation (Figure 1b), which will cause the loss of COFs during the preparation and operation of the membrane.[36] After being blended into the PAN solution, the monomers and the catalyst immediately dissolved and the color of the PAN solution turns from light yellow to dark purple with the addition of monomers (Figure 1c). The thus-prepared casting solution can keep its stability without precipitation for at least 4 weeks, revealing the advantage of this *in situ* growth strategy in preparing a stable COF-incorporated casting solution. In contrast to the white color of the PAN membrane (Figure 1d), the resulting TpEB−PAN membrane appears a uniform color of bright orange (Figure 1e), indicating the completion of the cocondensation reaction of the monomers as well as good dispersion of TpEB crystallites in the obtained membrane.

To confirm the condensation of Tp and EB to produce TpEB, we compared the FT-IR spectra of monomer pairs, synthesized COF particulates, and fabricated TpEB−PAN membranes. As illustrated in Figure 2a, the FT-IR spectra of the TpEB particulates show the disappearance of characteristic absorption peaks of the N−H stretching bands (3185, 3309 cm^{-1}) of EB and the aldehyde group stretching bands (1630 cm^{-1}) of Tp, implying the complete consumption of monomers. Further, the C−N stretching bands (1248 cm^{-1}) and the C═C bands (1593 cm^{-1}) demonstrate the successful formation of TpEB.[33] As for TpEB−PAN membranes, due to the existence of abundant C−N bonds on the PAN structure, the absorption peaks for C−N bonds overlap.[24,25] However, when deliberately increasing the amount of monomer pairs in

https://dx.doi.org/10.1021/acs.langmuir.0c01714
Langmuir 2020, 36, 10970−10978

the casting solution to 1 wt %, the C=C stretching bands of the resultant membrane can be clearly detected (Figure 2a), which gives the proof of the reaction to produce TpEB. EDS mapping results (Figure S1) also verify that the O and Br elements, which only stably exist in TpEB, can be detected on the membrane surface, demonstrating the formation of TpEB in the membrane. For XRD characterization, the pattern of TpEB particulates exhibits an intense diffraction peak at 3.3° and a broad peak at 27° (Figure S2a), corresponding to the (100) and (001) reflections, respectively.[34] The result indicates that the synthesized TpEB particulates possess the desirable crystallinity. We did not observe noticeable diffraction peaks from the XRD pattern of the TpEB−PAN membrane because the ultralow amount (<0.1 wt %) of TpEB can be hardly detected in this case (Figure S3). Therefore, we dissolved the TpEB−PAN membrane in DMF and collected TpEB nanoparticles by filtration for XRD characterizations. As shown in Figure 2b, the diffraction peaks at ∼3.4 and ∼28° can be assigned to the (100) and (001) planes, revealing the moderate crystallinity of TpEB in the membrane. Furthermore, as can be seen from Figure 2c,d, the $TpEB_5$−PAN membrane shows a significantly enhanced fluorescence intensity compared to the PAN membrane, which serves as another evidence for the successful formation of TpEB in the prepared membrane.[37,38]

A series of characterizations were carried out to reveal the mediating effect of cationic TpEB during membrane preparation, with results given in Figures 3 and 4. We first

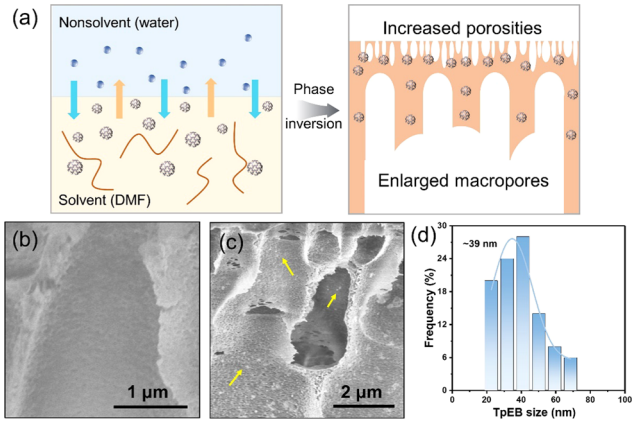

Figure 4. Investigation into the formation mechanism of highly porous TpEB−PAN membranes. (a) Illustration of the formation of TpEB−PAN membranes, cross-sectional morphologies of the (b) PAN membrane and (c) $TpEB_5$−PAN membrane, and (d) size distribution of TpEB crystallites incorporated into the $TpEB_5$−PAN membrane.

observed the surface morphology of the TpEB−PAN membranes. As shown in Figure 3a, the original PAN membrane has a typical nanoporous morphology of the ultrafiltration membrane prepared by NIPS. With the *in situ* growth of TpEB, the surface pore density and average pore sizes of the TpEB−PAN membranes are obviously increased (Figures 3a and S4), demonstrating that the mediation of TpEB in the fabrication of TpEB−PAN membranes is realized. As shown in Figure 3b, the original PAN membrane has a surface pore density of 63 pores μm^{-2}. After blending the monomer pairs with an ultralow concentration of 0.03 wt %, there is a 132% increase of pore density on the membrane surface, which reaches 146 pores μm^{-2}. The pore density of the $TpEB_5$−PAN membrane triples compared to that of the original PAN membrane, coming to 196 pores μm^{-2}. A further increase of the monomer amount leads to a slight decline in the pore density. For instance, when the amount of monomer pairs comes to 0.09 wt %, the pore density drops to 175 pores μm^{-2}, but it is still greatly higher than that of the original PAN membrane (63 pores μm^{-2}). The significantly increased pore density offers more mass transfer routes, facilitating the permeation of water to deliver improved performance in return.[25] Also, the pore size distributions of the membranes demonstrate that there is a slight increase in the average pore size (Figure 3c). Specifically, the average pore size increases from ∼10 nm for the original PAN membrane to ∼15 nm for the $TpEB_3$−PAN membrane and maintains ∼20 nm when the monomer amount reaches 0.09 wt %. The increase in the surface pore density along with the larger pore sizes on the membrane surface results from the modulating effect of TpEB crystallites in the membrane. Cationic TpEB delivers an intrinsic nature of high hydrophilicity and possesses a strong interaction with water molecules. Therefore, the grown TpEB crystallites will migrate onto the membrane surface during the NIPS process when choosing water as the coagulation bath,[26] which is also verified by the EDS mapping results (Figure S1). The high hydrophilicity of TpEB crystallites can significantly accelerate the exchange rate between the solvent (DMF) and the nonsolvent (water). The dominant passways for water permeance are still the pores of the polymer matrix generated *via* phase inversion. The intrinsic pores of TpEB (1.7 nm in size[33]), although very low in total amount, also help to open up more passways for water permeation.[24,25] This synergetic effect of TpEB makes it easier for water molecules to penetrate through the nascent membrane, leading to the rapid formation of a highly porous surface (Figure 4a).[39−41] Notably, the monomer pairs, Tp and EB, are small organic molecules, which are much smaller than the pore size (∼10 to 20 nm) and the thickness (∼150 to 200 μm) of the TpEB−PAN membranes. Therefore, the adoption of Tp and EB for *in situ* growth will not do harm to membrane porosity. We also investigated the surface roughness of the membranes and a distinguished increase can be observed (Figures 3d and S5). The original PAN membrane has an arithmetic average roughness (R_a) value of 5.1 nm, while the R_a value of the $TpEB_5$−PAN membrane dramatically increases to 16.8 nm. The results match well with the migration of TpEB onto the membrane surface, as discussed above.

To gain more insight into the mediating roles of TpEB in the NIPS process (Figure 4a), we then examined the changes of cross-sectional morphology of the self-standing TpEB−PAN membranes with various monomer concentrations. Different from the original PAN membrane, we can clearly observe the presence of TpEB crystallites on the pore walls of the $TpEB_5$−PAN membrane, which have an average size of ∼39 nm (Figure 4b−d). This structural difference illustrates the successful incorporation of nanosized TpEB crystallites into the PAN matrix. Obviously, the cross-sectional morphology of the membranes can be divided into two layers: the top layer and the sublayer (Figure S6). At the top layer of the membrane, we can observe relatively regular fingerlike macropores. The pores become larger with an increase of membrane depth, and loose macrovoids appear at the sublayer. Interestingly, the size of the macrovoids at the sublayer becomes larger with an increase of monomer concentrations.

https://dx.doi.org/10.1021/acs.langmuir.0c01714
Langmuir 2020, 36, 10970−10978

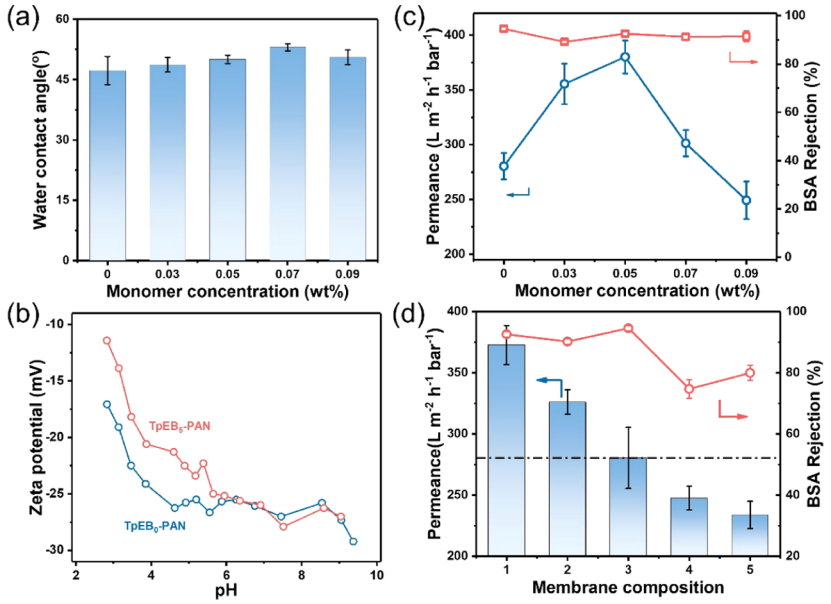

Figure 5. Surface properties and separation performances of the membranes. Water contact angles (a), ζ-potentials (b), and separation performances (c) of the TpEB−PAN membranes and (d) separation performances of membranes prepared with different COFs and strategies: *in situ* growth of TpEB (1), TpPa (4), TpBD, (5) crystallites, (2) postaddition of TpEB particulates, ad (3) without COFs.

This can be attributed to the slow solvent transfer rate in the sublayer caused by the high viscosity of the casting solution. The electrostatic attraction between cationic TpEB and negatively charged PAN chains results in the formation of the PAN matrix consisting of PAN chains with cationic TpEB as "pendant" groups, which significantly increases the viscosity of the casting solution.[42,43] After the rapid penetration of water molecules through the membrane surface into the sublayer, the movement is hindered by the high viscosity of the bulk of the casting solution. Thus, the exchange rate of the solvent and nonsolvent decreases and the PAN precipitates more slowly in the sublayer. Due to the slow viscous fingering of water molecules into the bulk of the casting solution, macrovoids form with larger sizes (Figure 4a). It is worth noting that while the expanded pores in the sublayer will facilitate water permeation to give improved permeance, the formation of aggregated regions caused by the increase of TpEB in the membranes will lead to higher transfer resistance to decrease the water permeance.[24] Thus, it is necessary to balance the above-mentioned tradeoff to acquire a satisfying separation performance.

Before the filtration tests, we measured the water contact angle (WCA) of TpEB−PAN membranes to determine their hydrophilicity, which plays a great role in the water permeation of ultrafiltration membranes. As shown in Figure 5a, although slightly increasing from 47 to 53°, the WCAs of TpEB−PAN membranes and the PAN membrane are about 50° and basically unchanged, which means the membranes are hydrophilic enough to allow water molecules to easily permeate through. The surface charges were clarified by the characterization of the ζ-potential of the membrane surfaces. As can be seen from Figure 5b, there is a decrease in negative charge on the membrane surface, which can be ascribed to the migration of the positively charged TpEB onto the membrane surface to offset part of the negative charges. Then, we investigated the separation performances of the membranes, with results given in Figure 5c. The original PAN membrane shows pure water permeance of 280.3 L m^{-2} h^{-1} bar^{-1} and a BSA rejection of 94.6%. With the incorporation of an ultralow monomer amount of 0.03 wt %, the permeance of the $TpEB_3$−PAN membrane significantly increases to 355.5 L m^{-2} h^{-1} bar^{-1}, as well as maintains a BSA rejection of 90.1%. The permeance of the $TpEB_5$−PAN membrane further increases to 380.1 L m^{-2} h^{-1} bar^{-1} with a 92.6% of BSA rejection. There is a noticeable decrease in the permeance values when the amounts of monomers increase to 0.07 and 0.09 wt %, which are 301.4 and 249.2 L m^{-2} h^{-1} bar^{-1}, respectively. In these cases, the BSA rejection remains above 90%. The trend of performance change matches well with the characterizations stated above. With an increase of TpEB in the membrane, more and slightly bigger pores generate on the membrane surface, which explains the increase in water permeance. When the amounts of monomers reach 0.07 and 0.09 wt %, the surface pore density and average pore sizes remain basically unchanged, but there is a significant decline in the water permeance. This is probably due to the increase in mass transfer resistance caused by the formation of aggregated regions in the membrane with higher TpEB concentrations.[24]

To show the advantage of this *in situ* growth strategy for producing COF-based MMMs using cationic TpEB, the ultrafiltration performances of the membranes fabricated by postadding TpEB particulates and *in situ* growth of negatively charged TpPa[37] and TpBD[44] were also investigated, with results shown in Figure 5d. Membranes fabricated by the *in situ* growth of TpEB crystallites and the postaddition of TpEB particulates both present improved permeances than the original PAN membranes and deliver high rejections to BSA. On the contrary, the membranes with *in situ* synthesized TpPa and TpBD show much decreased water permeance values and remarkably lower BSA rejections. To be specific, the membrane with the postaddition of 0.05 wt % TpEB particulates shows water permeance of 326.1 L m^{-2} h^{-1} bar^{-1}, which is 16.5% higher than that of the original PAN membrane but still much lower than that of the $TpEB_5$−PAN membrane (380.1 L m^{-2} h^{-1} bar^{-1}). The membranes with *in situ* growth of negatively charged TpPa and TpEB show water

https://dx.doi.org/10.1021/acs.langmuir.0c01714
Langmuir 2020, 36, 10970−10978

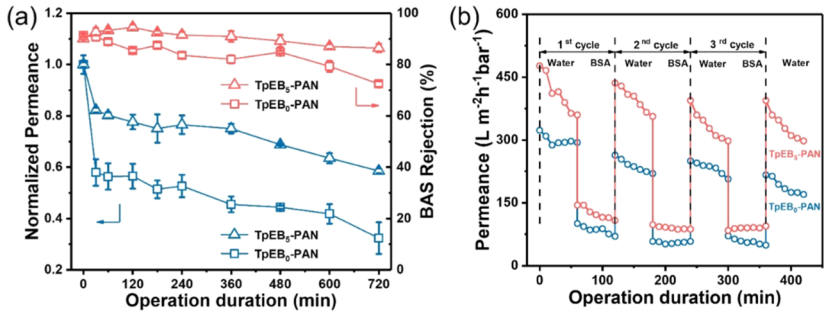

Figure 6. Study on the stability of the PAN and $TpEB_5$–PAN membranes. (a) Operation stability and (b) fouling resistance.

permeance values of 247.4 and 233.7 L m^{-2} h^{-1} bar^{-1} and BSA rejections of 74.7 and 79.9%, respectively. As illustrated above, in the *in situ* growth strategy, the growth of TpEB crystallines is inhibited due to the interaction with PAN chains, leading to the formation of a well-dispersed, homogeneous, nanosized, TpEB-incorporated casting solution without the interference of aggregation or sedimentation.[35,36] However, the relatively larger size of TpEB particulates (Figure S2b) adopted in the postaddition method decreases the stability of the casting solution and makes TpEB particulates easier for agglomeration, as well as weakens their affinity and attachment to PAN chains. The *in situ* synthesized TpPa and TpBD repel the PAN chains because they both bear negative charges, and the growth of these COFs is not restrained, leading to the generation of oversized COF particulates, which is similar to the postaddition method. In general, the TpEB–PAN membrane prepared by *in situ* growth of cationic TpEB crystallites shows greatly improved ultrafiltration performance, which demonstrates a facile protocol for the preparation of advanced ultrafiltration MMMs. Furthermore, similar to the addition of other modifiers or fillers, this *in situ* growth strategy does not change the basis of the NIPS process and therefore has great potential for scalable production.

We also compared the stability of the original PAN membrane to that of the $TpEB_5$–PAN membrane, with results shown in Figures 6 and S7. After ultrafiltration for 6 h, the $TpEB_5$–PAN membrane exhibits water permeance of 75% compared to the beginning permeance and shows a BSA rejection of 91%, while the PAN membrane only shows 45 and 82%, respectively. At the end of the test, the permeance of the $TpEB_5$–PAN membrane reduces to 59% of its original permeance, while that of the PAN membrane falls dramatically to less than 30%. Hence, the $TpEB_5$–PAN membrane exhibits better long-term stability than the original PAN membrane, which may originate from the enhanced mechanical stability provided by the robust TpEB crystallites. Figure 6b illustrates the time-dependent membrane permeance of the original PAN membrane and the $TpEB_5$–PAN membrane by ultrafiltering deionized water and BSA solution alternately for three cycles. Throughout the test, the TpEB–PAN membrane shows higher permeance for pure water as well as BSA solution than the PAN membrane. For instance, the $TpEB_5$–PAN membrane holds initial water permeance of 359.8 L m^{-2} h^{-1} bar^{-1}. After being fouled by BSA, the permeance reduces to 108.1 L m^{-2} h^{-1} bar^{-1}. After being cleaned by water, it recovers the permeance to 356.1 L m^{-2} h^{-1} bar^{-1}, indicating an FRR value of 99.0%. As a comparison, the permeance of the original PAN membrane significantly decreases from 293.7 to 70.1 L m^{-2} h^{-1} bar^{-1} once fouled by BSA and the FRR value after the first cycle is only 74.9%. Notably, the FRR values of the $TpEB_5$–PAN membrane and the original PAN membrane after the second and third cycles are 82.8, 82.7%, and 70.4, 57.9%, respectively, demonstrating a significant enhanced antifouling competence of the TpEB–PAN membranes. This enhancement can be attributed to the difference in surface charge of the membranes. The positively charged TpEB on the membrane surface weakens the adsorption of BSA, making the TpEB–PAN membrane easier to recover its water permeance after fouling.

CONCLUSIONS

In summary, we have developed a facile *in situ* growth strategy to improve the performance of polymer ultrafiltration membranes. A cationic COF of TpEB with a size down to ~39 nm is *in situ* synthesized in the PAN solution by blending monomers and catalysts in the casting solution to produce TpEB–PAN membranes. Bearing opposite charges, the cationic TpEB crystallites and the negatively charged PAN chains interact with each other *via* electrostatic interaction, leading to a well-dispersed, homogeneous TpEB-incorporated casting solution. The TpEB crystallites serve as both functional fillers and modulators to regulate the NIPS process, improving the rate of demixing between the solvent and nonsolvent to improve membrane porosities. Because of the high hydrophilicity of TpEB, it can migrate onto the membrane surface, generating more pores to improve the membrane permeance. As a result, the $TpEB_5$–PAN membrane shows pure water permeance of 380.1 L m^{-2} h^{-1} bar^{-1}, which is 35.6% higher than that of the original PAN membranes in the absence of TpEB, while retaining a high BSA rejection of 92.6%. Apart from the increased water permeance, thus-prepared TpEB–PAN membranes also exhibit improved operation stability and antifouling competence. The *in situ* growth strategy presented in this work shows its superiority in the preparation of ultrafiltration MMMs with enhanced performances. This strategy is expected to extend its application in the production of highly permeable membranes using other nanoporous materials, such as metal–organic frameworks (MOFs) and polymers of intrinsic microporosity (PIMs).

ASSOCIATED CONTENT

Supporting Information

The Supporting Information is available free of charge at https://pubs.acs.org/doi/10.1021/acs.langmuir.0c01714.

EDS mapping of the TpEB–PAN membrane with 1 wt % monomer pairs in the casting solution, characterizations of the TpEB particulates synthesized by the thermal solvent method, XRD patterns of the $TpEB_9$–PAN membrane and PAN membrane, surface morphol-

https://dx.doi.org/10.1021/acs.langmuir.0c01714
Langmuir 2020, 36, 10970–10978

ogy of the $TpEB_9$–PAN membrane, AFM topologies of the TpEB–PAN membranes with various monomer concentrations, cross-sectional morphologies of the self-standing TpEB–PAN membranes with various monomer concentrations, and long-term stability of the $TpEB_5$–PAN and PAN membrane (PDF)

AUTHOR INFORMATION

Corresponding Author

Yong Wang − *State Key Laboratory of Materials-Oriented Chemical Engineering and College of Chemical Engineering, Nanjing Tech University, Nanjing 211816, P. R. China;* orcid.org/0000-0002-8653-514X; Email: yongwang@njtech.edu.cn

Authors

Xingyuan Wang − *State Key Laboratory of Materials-Oriented Chemical Engineering and College of Chemical Engineering, Nanjing Tech University, Nanjing 211816, P. R. China*

Xiansong Shi − *State Key Laboratory of Materials-Oriented Chemical Engineering and College of Chemical Engineering, Nanjing Tech University, Nanjing 211816, P. R. China*

Complete contact information is available at: https://pubs.acs.org/10.1021/acs.langmuir.0c01714

Author Contributions

The manuscript was written through the contribution of all authors. All authors have given approval to the final version of the manuscript.

Notes

The authors declare no competing financial interest.

ACKNOWLEDGMENTS

Financial support from the National Science Fund for Distinguished Young Scholars (21825803) is gratefully acknowledged. We also thank the Program of Excellent Innovation Teams of Jiangsu Higher Education Institutions and the Project of Priority Academic Program Development of Jiangsu Higher Education Institutions (PAPD).

REFERENCES

(1) Côté, A. P.; Benin, A. I.; Ockwig, N. W.; O'Keeffe, M.; Matzger, A. J.; Yaghi, O. M. Porous, crystalline, covalent organic frameworks. *Science* **2005**, *310*, 1166−1170.

(2) Wang, J. X.; Li, J.; Gao, M. X.; Zhang, X. M. Recent advances in covalent organic frameworks for separation and analysis of complex samples. *TrAC, Trends Anal. Chem.* **2018**, *108*, 98−109.

(3) Uribe-Romo, F. J.; Doonan, C. J.; Furukawa, H.; Oisaki, K.; Yaghi, O. M. Crystalline covalent organic frameworks with hydrazone linkages. *J. Am. Chem. Soc.* **2011**, *133*, 11478−11481.

(4) Segura, J. L.; Mancheñoa, M. J.; Zamora, F. Covalent organic frameworks based on Schiff-base chemistry: synthesis, properties and potential applications. *Chem. Soc. Rev.* **2016**, *45*, 5635−5671.

(5) Jin, E. Q.; Asada, M.; Xu, Q.; Dalapati, S.; Addicoat, M. A.; Brady, M. A.; Xu, H.; Nakamura, T.; Heine, T.; Chen, Q. H.; Jiang, D. L. Two-dimensional sp^2 carbon-conjugated covalent organic frameworks. *Science* **2017**, *357*, 673−676.

(6) Kandambeth, S.; Mallick, A.; Lukose, B.; Mane, M. V.; Heine, T.; Banerjee, R. Construction of crystalline 2D covalent organic frameworks with remarkable chemical (acid/base) stability via a combined reversible and irreversible route. *J. Am. Chem. Soc.* **2012**, *134*, 19524−19527.

(7) Wu, D. C.; Xu, F.; Sun, B.; Fu, R. W.; He, H. K.; Matyjaszewski, K. Design and preparation of porous polymers. *Chem. Rev.* **2012**, *112*, 3959.

(8) Xiang, Z. H.; Cao, D. P.; Dai, L. M. Well-defined two-dimensional covalent organic polymers: rational design, controlled syntheses, and potential applications. *Polym. Chem.* **2015**, *6*, 1896.

(9) Rogge, S. M.; Bavykina, A.; Hajek, J.; Garcia, H.; Olivos-Suarez, A. I.; Sepúlveda-Escribano, A.; Vimont, A.; Clet, G.; Bazin, P.; Kapteijn, F.; Daturi, M.; Ramos-Fernandez, E. V.; Llabres, F. X.; Speybroeck, V. V.; Gascon, J. Metal-organic and covalent organic frameworks as single-site catalysts. *Chem. Soc. Rev.* **2017**, *46*, 3134−3184.

(10) Wang, X.; Ye, N. S. Recent advances in metal-organic frameworks and covalent organic frameworks for sample preparation and chromatographic analysis. *Electrophoresis* **2017**, *38*, 3059−3078.

(11) Biswal, B. P.; Chaudhari, H. D.; Banerjee, R.; Kharul, U. K. Chemically stable covalent organic framework (COF)-polybenzimidazole hybrid membranes: enhanced gas separation through pore modulation. *Chem. - Eur. J.* **2016**, *22*, 4695.

(12) Kandambeth, S.; Biswal, B. P.; Chaudhari, H. D.; Rout, K. C.; Kunjattu, S.; Mitra, S.; Karak, S.; Das, A.; Mukherjee, R.; Kharul, U. K.; Banerjee, R. Selective molecular sieving in self-standing porous covalent-organic-framework membranes. *Adv. Mater.* **2017**, *29*, No. 1603945.

(13) Zhou, Z. M.; Zhong, W. F.; Cui, K. X.; Zhuang, Z. Y.; Li, L. Y.; Li, L. Y.; Bi, J. H.; Yu, Y. A covalent organic framework bearing thioether pendant arms for selective detection and recovery of Au from ultra-low concentration aqueous solution. *Chem. Commun.* **2018**, *54*, 9977.

(14) Doonan, C. J.; Tranchemontagne, D. J.; Glover, T. G.; Hunt, J. R.; Yaghi, O. M. Exceptional ammonia uptake by a covalent organic framework. *Nat. Chem.* **2010**, *2*, 235.

(15) Shi, X. S.; Ma, D. W.; Xu, F.; Zhang, Z.; Wang, Y. Table-salt enabled interface-confined synthesis of covalent organic framework (COF) nanosheets. *Chem. Sci.* **2020**, *11*, 989.

(16) Matsumoto, M.; Valentino, L.; Stiehl, G. M.; Balch, H. B.; Corcos, A. R.; Wang, F.; Ralph, D. C.; Marinas, B. J.; Dichtel, W. R. Lewis-Acid-Catalyzed Interfacial Polymerization of Covalent Organic Framework Films. *Chem* **2018**, *4*, 308−317.

(17) Zhang, K.; He, Z.; Gupta, K. M.; Jiang, J. Computational design of 2D functional covalent-organic framework membranes for water desalination. *Environ. Sci.: Water Res. Technol.* **2017**, *3*, 735−743.

(18) Zhang, L. L.; Wang, L.; Wang, N. X.; Guo, H. X.; Zhang, W. H.; Li, X. T.; Ji, S. L.; An, Q. F. Covalent organic frameworks hybird membrane with optimized mass transport nanochannel for aromatic/aliphatic mixture pervaporation. *J. Membr. Sci.* **2020**, *598*, No. 117652.

(19) Fan, H.; Gu, J.; Meng, H.; Knebel, A.; Caro, J. High-flux imine-linked covalent organic framework COF-LZU1 membranes on tubular alumina supports for highly selective dye separation by nanofiltration. *Angew. Chem., Int. Ed.* **2018**, *57*, 4083−4087.

(20) Dey, K.; Pal, M.; Rout, K. C.; Kunjattu, S.; Das, A.; Mukherjee, R.; Kharul, U. K.; Banerjee, R. Selective molecular separation by interfacially crystallized covalent organic framework thin films. *J. Am. Chem. Soc.* **2017**, *139*, 13083−13091.

(21) Ulbricht, M. Advanced functional polymer membranes. *Polymer* **2006**, *47*, 2217−2262.

(22) Yuan, S. S.; Li, X.; Zhu, J. Y.; Zhang, G.; Puyvelde, P. V.; Bruggen, B. V. Covalent organic frameworks for membrane separation. *Chem. Soc. Rev.* **2019**, *48*, 2665−2681.

(23) Yang, H.; Cheng, X. P.; Cheng, X. X.; Pan, F. S.; Wu, H.; Liu, G. H.; Song, Y. M.; Cao, X. Z.; Jiang, Z. Y. Highly water-selective membranes based on hollow covalent organic frameworks with fast transport pathways. *J. Membr. Sci.* **2018**, *565*, 331−341.

(24) Duong, P. H.; Kuehl, V. A.; Li-Oakey, K. D.; Mastorovich, B.; Hoberg, J. O.; Parkinson, B. A. Carboxyl-functionalized covalent organic framework as a two-dimensional nanofiller for mixed-matrix ultrafiltration membranes. *J. Membr. Sci.* **2019**, *574*, 338−348.

(25) Xu, L. N.; Xu, J.; Shan, B.; Wang, X. L.; Gao, C. J. TpPa-2-incorporated mixed matrix membranes for efficient water purification. *J. Membr. Sci.* **2017**, *526*, 355−366.
(26) Wang, D. M.; Lai, J. Y. Recent advances in preparation and morphology control of polymeric membranes formed by nonsolvent induced phase separation. *Curr. Opin. Chem. Eng.* **2013**, *2*, 229−237.
(27) Strathmann, H.; Kock, K.; Amar, P.; Baker, R. W. The formation mechanism of asymmetric membranes. *Desalination* **1975**, *16*, 179−203.
(28) Lee, H. Y.; Krantz, W. B.; Hwang, S. T. A model for wet-casting polymeric membranes incorporating nonequilibrium interfacial dynamics, vitrification and convection. *J. Membr. Sci.* **2010**, *354*, 74−85.
(29) Guillen, G. R.; Pan, Y. J.; Li, M. H.; Hoek, M. V. Preparation and characterization of membranes formed by nonsolvent induced phase separation: A review. *Ind. Eng. Chem. Res.* **2011**, *50*, 3798−3817.
(30) Liu, F.; Hashim, N. A.; Liu, Y. T.; Abed, R. M.; Li, K. Progress in the production and modification of PVDF membranes. *J. Membr. Sci.* **2011**, *375*, 1−27.
(31) Yin, J.; Deng, B. L. Polymer-matrix nanocomposite membranes for water treatment. *J. Membr. Sci.* **2015**, *479*, 256−275.
(32) Kertik, A.; Khan, A.; Vankelecom, I. Metal organic framework containing mixed matrix membranes for gas separation: a different approach to MMM preparation methods. *Procedia Eng.* **2012**, *44*, 106−107.
(33) Ma, H. P.; Liu, B. L.; Li, B.; Zhang, L. M.; Li, Y. G.; Tan, H. Q.; Zang, H. Y.; Zhu, G. S. Cationic covalent organic frameworks: a simple platform of anionic exchange for pore density tuning and proton conduction. *J. Am. Chem. Soc.* **2016**, *138*, 5897−5903.
(34) Zhang, W. X.; Zhang, L. M.; Zhao, H. F.; Li, B.; Ma, H. P. A two-dimensional cationic covalent organic framework membrane for selective molecular sieving. *J. Mater. Chem. A* **2018**, *6*, 13331−13339.
(35) Zhang, Q.; Chai, Y. Y.; Cao, M. T.; Yang, F. L.; Zhang, L.; Dai, W. L. Facile synthesis of ultra-small Ag decorated g-C_3N_4 photocatalyst via strong interaction between Ag^+ and cyano group in monocyanamide. *Appl. Surf. Sci.* **2020**, *503*, No. 143891.
(36) Wu, G. R.; Li, Y. L.; Geng, Y. Z.; Jia, Z. Q. In-situ preparation of COF-LZU1 in poly(ether-block-amide) membranes for efficient pervaporation of n-butanol/water mixture. *J. Membr. Sci.* **2019**, *581*, 1−8.
(37) Wang, R.; Shi, X. S.; Zhang, Z.; Xiao, A. K.; Sun, S. P.; Cui, Z. L.; Wang, Y. Unidirectional diffusion synthesis of covalent organic frameworks (COFs) on polymeric substrates for dye separation. *J. Membr. Sci.* **2019**, *586*, 274−280.
(38) Shi, X. S.; Wang, R.; Xiao, A. K.; Jia, T. Z.; Sun, S. P.; Wang, Y. Layer-by-layer synthesis of covalent organic frameworks on porous substrates for fast molecular separations. *ACS Appl. Nano Mater.* **2018**, *1*, 6320−6326.
(39) Idris, A.; Ahmed, I.; Misran, M. Novel high performance hollow fiber ultrafiltration membranes spun from LiBr doped solutions. *Desalination* **2009**, *249*, 541−548.
(40) Wang, D.; Li, K.; Teo, W. Porous PVDF asymmetric hollow fiber membranes prepared with the use of small molecular additives. *J. Membr. Sci.* **2000**, *178*, 13−23.
(41) Shi, L.; Wang, R.; Cao, Y.; Liang, D. T.; Tay, J. H. Effect of additives on the fabrication of poly (vinylidene fluoride-co-hexafluoropropylene) (PVDF-HFP) asymmetric microporous hollow fiber membranes. *J. Membr. Sci.* **2008**, *315*, 195−204.
(42) Bottino, A.; Capannelli, G.; Munari, S.; Turturro, A. High performance ultrafiltration membranes cast from LiCl doped solutions. *Desalination* **1988**, *68*, 167−177.
(43) Tager, A.; Dreval, Y.; Serikov, A.; Surayeva, V. Effect of inorganic salt additives on the viscosity of cellulose acetate solutions. *Polym. Sci.* **1976**, *18*, 2163−2168.
(44) Wang, R.; Shi, X. S.; Xiao, A. K.; Zhou, W.; Wang, Y. Interfacial polymerization of covalent organic frameworks (COFs) on polymeric substrates for molecular separations. *J. Membr. Sci.* **2018**, *566*, 197−204.

https://dx.doi.org/10.1021/acs.langmuir.0c01714
Langmuir 2020, 36, 10970−10978